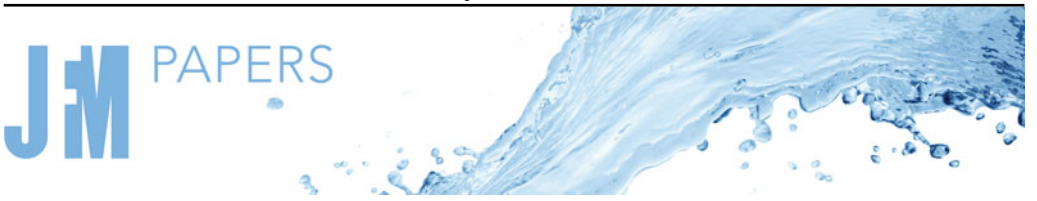
J. Fluid Mech. (2026), *vol.* 1032, A31, doi:10.1017/jfm.2026.11397



Lift force models for a spherical particle immersed in linear and quadratic shear flows

Tongkuai Wang[1], **Zhaowu Lin**[1], **Xiaoke Ku**[1] **and Zhaosheng Yu**[1]

[1]State Key Laboratory of Fluid Power and Mechatronic System, Department of Mechanics, Zhejiang University, Hangzhou 310027, PR China

Corresponding author: Zhaosheng Yu, yuzhaosheng@zju.edu.cn

(Received 22 July 2025; revised 27 February 2026; accepted 28 February 2026)

The lift force models for a particle in wall-bounded linear shear flow have been extensively investigated; however, the influence of the curvature of the velocity profile (Sg) on the lift force at finite slip Reynolds numbers (Re) remains unexplored. In the present work, direct numerical simulations (DNS) are performed to investigate the lift on a spherical particle in unbounded linear shear flow, single-wall-bounded linear shear flow and Poiseuille flow. Based on our DNS data, we first extend the existing unbounded and single-wall-bounded linear shear-slip-induced lift models to higher non-dimensional shear rates ($|Sr| = 2.5$) for $0.1 \leqslant Re \leqslant 20$. Based on the empirical model for Couette flow or the analytical model for unbounded Poiseuille flow, the lift models are then modified to account for the curvature effect of the parabolic velocity profile, which reduce to the linear shear-slip-induced lift models in the high Re and low Sg limits. We also modify the rotation-induced lift model of linear shear flow to account for the parabolic shear effect, which causes lift enhancement for the leading particle and lift attenuation for the lagging particle in the Poiseuille flow, compared to the linear shear case. This lift attenuation may give rise to an inverse Magnus force at low slip Reynolds numbers. In addition, the model for the particle free rotation rate for the Poiseuille flow is established by correcting the one for the linear shear flow, providing a more accurate prediction of the torque on the particle.

Key words: particle/fluid flow

1. Introduction

Particulate flows with confined boundaries and nonlinear background velocity fields are ubiquitous in both industrial and biological applications, e.g. deep-sea mining (Wei *et al.* 2023) and cell isolation (Hur *et al.* 2011). Hydrodynamic forces are the primary factors influencing particle motion and equilibrium position in dilute suspensions. Consequently, it is of practical importance to establish the lift force model for a spherical particle in Poiseuille flow.

© The Author(s), 2026. Published by Cambridge University Press.

https://doi.org/10.1017/jfm.2026.11397 Published online by Cambridge University Press

Since Segré & Silberberg (1961) experimentally observed that neutrally buoyant particles in pipe flow radially migrated to a position approximately 0.6 pipe radius away from the centreline, a considerable number of numerical studies have been devoted to the particle migration in the parabolic channel/tube flow (Yu, Phan-Thien & Tanner 2004; Yang *et al.* 2005; Shao, Yu & Sun 2008; Hood, Lee & Roper 2015; Asmolov *et al.* 2018; Nakayama *et al.* 2019). In the aspect of modelling, Yahiaoui & Feuillebois (2010) adopted the Lorentz reciprocity results of Ho & Leal (1974) to derive the migration velocity of an inertialess particle or the lift on a particle translating in a constant speed in a single-wall-bounded parabolic shear flow, and their models cover a wide range of particle–wall separation distances ($0.505 \leqslant L \leqslant 50$). Asmolov *et al.* (2018) noticed the importance of finite slip velocity to the particle equilibrium position, and proposed a model by combining the stresslet contribution from Vasseur & Cox (1976) and the Stokeslet contribution from Cherukat & Mclaughlin (1994). However, most of these models based on analytical solutions are restricted to either neutrally buoyant point particles (Ho & Leal 1974; Vasseur & Cox 1976; Schonberg & Hinch 1989; Asmolov 1999; Matas *et al.* 2004, 2009) or non-neutrally buoyant particles with $Re \ll 1$ (Re being the slip Reynolds number defined in (2.7)) (Vasseur & Cox 1976; Asmolov 1999; Matas, Morris & Guazzelli 2004).

For finite slip Reynolds numbers, the existing lift models are generally limited to either uniform or linear shear flows. For simple shear flow, Cherukat, McLaughlin & Dandy (1999) numerically validated the use of Saffman's leading two terms together with the rotation term to describe the lift on a free rotating sphere in linear shear flow up to $Re \sim O(1)$. Shi & Rzehak (2019) extended the Saffman lift model to $Re \leqslant 50$ based on the numerical data with $Sr \leqslant 0.8$ (Sr being the dimensionless shear rate defined in (2.7)) from the literature (Kurose & Komori 1999; Bagchi & Balachandar 2002; Kim 2006). However, discrepancies remain between different numerical results, and there is a lack of data for $Sr > 1$ in the literature. For single-wall-bounded uniform flow, an analytical solution for this lift was first derived by Vasseur & Cox (1977) for small but finite slip Reynolds numbers. This solution was later extended to the case of a spherical droplet of arbitrary viscosity ratio by Takemura *et al.* (2002), who found that, irrespective of the boundary conditions at the interface, the wall-induced lift is proportional to the square of the vorticity generated at the interface of the sphere. Based on this argument, the direct numerical simulations (DNS) data for the surface vorticity from Magnaudet, Rivero & Fabre (1995) and the experimental results for contaminated bubbles, the solution by Vasseur & Cox (1977) for a solid particle was extended up to $Re = 100$ by Takemura & Magnaudet (2003). The lift predicted by this extended expression agrees well with their experimental data for nearly spherical, fully contaminated bubbles (which behave like solid particles at the same Re) in the range $1 < Re < 100$. Zeng *et al.* (2009) modified this model to make it valid up to $Re = 200$ based on their spectral element simulation results. For single-wall-bounded linear shear flow, the empirical model of Zeng *et al.* (2009) for a stationary particle covers the ranges $1 < Re < 200$ and $0.5 < L \leqslant 4$ (where L is the dimensionless wall distance defined in (2.7)). Takemura, Magnaudet & Dimitrakopoulos (2009) proposed a semi-analytical model based on numerical fitting of theoretical results (McLaughlin 1993), which was validated by the experiment for $0.5 < Re < 1.5$. Later, Shi *et al.* (2021) empirically extended their model to $Re = 100$. The lift coefficients predicted by semi-analytical models, based on experimental and DNS results, have shown significant deviations from analytical predictions.

To address the gap in modelling the lift on a finite-size spherical particle translating at finite Re in plane Poiseuille flow, the semi-analytical models for the linear shear flow mentioned above rather than the analytical ones for the Poiseuille flow are adopted in the present study, since we are aiming to provide a general prediction at finite slip

https://doi.org/10.1017/jfm.2026.11397 Published online by Cambridge University Press

Reynolds numbers. The analytical model for the Poiseuille flow was mainly proposed for the neutrally buoyant particle with a small slip velocity and thereby a small slip Reynolds number. It cannot account for the finite Reynolds number effect, e.g. the equilibrium position can no longer be predicted by the Segre–Silberberg effect, but may be shifted to the channel centre at a small Reynolds number $Re = 0.1$ due to Saffman effect. For relatively high Reynolds numbers (e.g. $Re > 50$), experimental results of Bai *et al.* (2022) showed that the critical Reynolds number for the zero lift can be approximately predicted by the model of Zeng *et al.* (2009), indicating that the difference between linear- and parabolic-shear-induced lifts may diminish as Re increases. Based on the above observations, we develop our lift models for the Poiseuille flow by modifying the existing models that have been widely used for predicting the lift in linear shear flow, and mainly focus on the correction for $0.1 \leqslant Re \leqslant 20$ based on our numerical data.

Our aim is to develop the lift model for a particle in a Poiseuille channel flow. In addition to accounting for the curvature of the background flow, a particle near the wall experiences a significantly larger shear rate compared to that in the channel bulk region. The relatively small slip velocity also results in a high Sr. As discussed by Gao *et al.* (2024), small inertial particles can experience a change in the sign of the slip velocity in wall turbulence, causing the slip velocity to be vanishingly small and Sr to increase dramatically. For a particle with large size or small density ratio, $Sr \geqslant 1$ can be easily reached according to the definition of Sr. Although the lift model for a spherical particle experiencing a finite slip velocity in single-wall-bounded linear shear flow has been investigated numerically (Lee & Balachandar 2010; Ekanayake, Berry & Harvie 2021; Shi *et al.* 2021), the works on the model for a wide range of Sr values are limited. The model proposed by Ekanayake *et al.* (2021) covers $0.02 \leqslant Sr \leqslant 200$, but is restricted to low slip Reynolds numbers ($0.002 \leqslant Re \leqslant 0.2$). The relatively high shear rate ($Sr = 1/L$) in the model of Zeng *et al.* (2009) decreases rapidly as the separation distance increases. Therefore, the lift models in the unbounded and single-wall-bounded linear shear need to be extended to higher Sr at finite Re.

The rest of the paper is organised as follows. We introduce the problem and the numerical method briefly in § 2. Numerical results and empirical models for the lift coefficient of a non-rotating particle in the unbounded linear shear flow, single-wall-bounded linear shear flow and plane Poiseuille flow are presented in §§ 3.1–3.3, respectively. The results for the rotation-induced lift force and the torque on a rotating particle in single-wall-bounded linear shear flow and Poiseuille flow are discussed in § 3.4. Concluding remarks are given in the final section.

2. Problem description and numerical method

Here, we consider a rigid spherical particle with diameter d moving in a channel of half-width h. Three flow configurations are considered in the present simulation: unbounded linear shear flow, single-wall-bounded linear shear flow, and plane Poiseuille flow, as shown in figure 1. The first two configurations are modelled as Couette flow, with one or two plane walls placed sufficiently far from the particle. The origin of Cartesian coordinates is located at the centre of the sphere and translates with the sphere at $\boldsymbol{u}_p = u_p \boldsymbol{e_x}$ parallel to the plane wall. The particle slip velocity is $\boldsymbol{u}_{slip} = \boldsymbol{u}_f|_{y=0} - \boldsymbol{u}_p$, where $\boldsymbol{u}_f$ is the undisturbed flow velocity. By introducing $\dot{\gamma}$ as the shear rate of the background flow, the undisturbed velocity field in the moving reference can be expressed as $\boldsymbol{u}_f = (\dot{\gamma} y + u_{slip})\boldsymbol{e_x}$ for a plane Couette flow, and $\boldsymbol{u}_f = (-\dot{\gamma} y^2/(2(h-l)) + \dot{\gamma} y + u_{slip})\boldsymbol{e_x}$ for plane Poiseuille flow. The near side wall is at distance l away from the particle centre.

https://doi.org/10.1017/jfm.2026.11397 Published online by Cambridge University Press

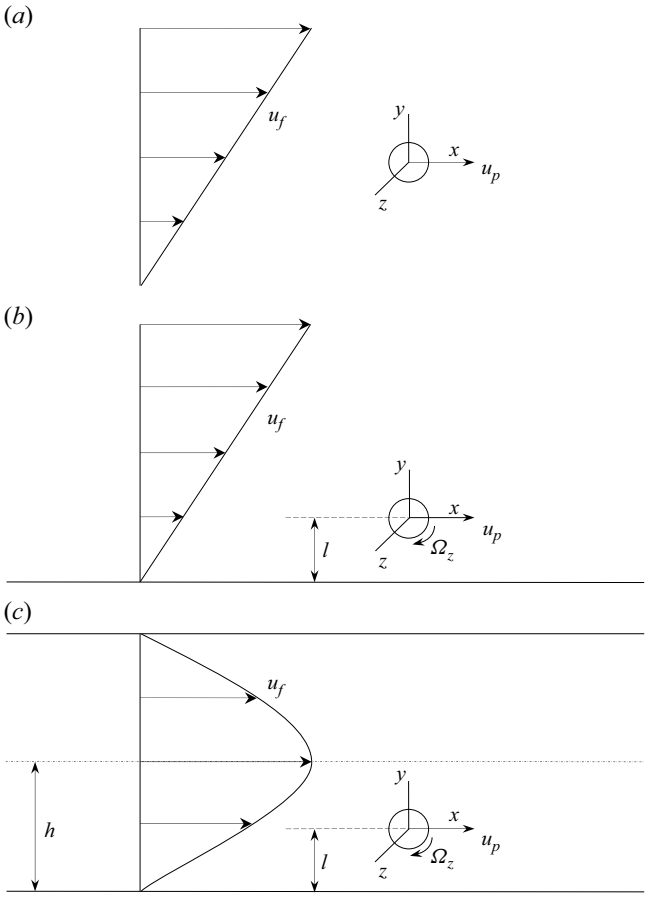


Figure 1. Schematics of a particle in (*a*) unbounded linear shear flow, (*b*) single-wall-bounded linear shear flow, and (*c*) plane Poiseuille flow.

The governing equations for the incompressible flow follow

$$\nabla \cdot \boldsymbol{u} = 0, \tag{2.1}$$

$$\frac{\partial \boldsymbol{u}}{\partial t} + \boldsymbol{u} \cdot \nabla \boldsymbol{u} = -\frac{1}{\rho}\nabla p + \nu \nabla^2 \boldsymbol{u}. \tag{2.2}$$

The boundary conditions in the moving reference frame are

$$\boldsymbol{u} = \left(-\frac{K\dot{\gamma} y^2}{2\,(h-l)} + \dot{\gamma} y + u_{slip}\right)\boldsymbol{e_x} \quad \text{for} \quad y = -l,\ y = 2h - l,\ |\boldsymbol{r}| = +\infty, \tag{2.3}$$

$$\boldsymbol{u} = \boldsymbol{\Omega} \times \boldsymbol{r} \quad \text{for} \quad |\boldsymbol{r}| = d/2, \tag{2.4}$$

where $K = 0$ ($K = 1$) for Couette (Poiseuille) flow, $\boldsymbol{r}$ is the position vector with respect to the centre of the particle, and $\boldsymbol{\Omega}$ is the angular velocity of the particle. The no-slip boundary conditions are imposed on the side walls and the particle surface.

https://doi.org/10.1017/jfm.2026.11397 Published online by Cambridge University Press

The lift and the torque can be calculated by integrating the pressure and viscous force on the particle surface, and the corresponding coefficients can be defined by

$$C_L = \frac{F_L}{\frac{1}{8}\pi d^2 \rho u_{slip}^2} = \frac{8}{\pi}\int_S (-p\boldsymbol{n} + \boldsymbol{n}\cdot\boldsymbol{\tau})\cdot\boldsymbol{e_y}\,\mathrm{d}s, \tag{2.5}$$

$$C_T = \frac{T_z}{\frac{1}{16}\pi d^3 \rho u_{slip}^2} = \frac{16}{\pi}\int_S (\boldsymbol{r}\times\boldsymbol{\tau}\cdot\boldsymbol{n})\cdot\boldsymbol{e_z}\,\mathrm{d}s, \tag{2.6}$$

where $\boldsymbol{\tau}$ is the viscous stress tensor.

The present problem of a particle in a channel flow involves eight independent physical quantities, including slip velocity u_{slip}, shear rate $\dot{\gamma}$, particle rotational velocity Ω_z, fluid density ρ, fluid viscosity ν, particle diameter d, channel half-width h, and distance between particle centre and near side wall l; therefore five dimensionless parameters are relevant. We choose d as the length scale and u_{slip} as the velocity scale, then five non-dimensional control parameters can be introduced as

$$Re = \frac{|u_{slip}|d}{\nu}, \quad Sr = \frac{\dot{\gamma}d}{u_{slip}}, \quad Rr = \frac{\Omega_z d}{u_{slip}}, \quad L = \frac{l}{d}, \quad H = \frac{h}{d}. \tag{2.7}$$

We keep the particle either stationary or rotating with angular velocity Ω_z about the z-axis, where Ω_z is positive for clockwise rotation, in the same direction as the ambient fluid's rotation with a positive shear rate. In the present study, we only consider a particle in the lower half-channel with a positive shear rate, and then a positive Sr implies a lagging sphere with a positive slip velocity, and a negative Sr implies a leading sphere with a negative slip velocity. We perform simulations with different parameter ranges depending on the specific flow configuration. For unbounded linear shear flow, the particle is fixed at the channel centre with $5 \leqslant Re \leqslant 20$ and $-2.5 \leqslant Sr \leqslant 2.5$. For single-wall-bounded linear shear flow, we choose $0.1 \leqslant Re \leqslant 20$, $-2.5 \leqslant Sr \leqslant 2.5$, $1 \leqslant L \leqslant 6$. For the Poiseuille flow, we choose $0.1 \leqslant Re \leqslant 100$, $1 \leqslant L \leqslant 6$, $4 \leqslant H \leqslant 12$ when $-0.5 \leqslant Sr \leqslant 0.5$, while for $0.5 < |Sr| \leqslant 2.5$, our data are limited to $0.1 \leqslant Re \leqslant 20$, $1 \leqslant L \leqslant 6$, $8 \leqslant H \leqslant 12$.

The open-source high-order spectral/hp element code Nektar++ (Cantwell *et al.* 2015) is employed to solve the Navier–Stokes equations. The way of partitioning the computational domain is the same as in our previous study (Wang *et al.* 2025). The effect of the polynomial order on the hydrodynamic forces has been examined for Couette flow in our previous study, which showed that $N_p = 5$ was required for $Re = 100$ and $Sr = 0.5$, while $N_p = 4$ was sufficient for $Re \leqslant 50$. We now provide the test results for the Poiseuille flow cases in table 1 according to the highest Re and $Re\,Sr$, which are also 100 and 50 in the present study, respectively. The polynomial order $N_p = 7$ is considered as the benchmark to compute the relative error δ in the table. In the following study, we still employ the polynomial order $N_p = 4$ for $Re \leqslant 50$, and $N_p = 5$ for higher Re, since the choices could ensure a relative error below 1.5 %.

For the wall-bounded case, we adopt the same size of the computational domain as in our previous study on Couette flow (Wang *et al.* 2025) to minimise the effect from boundary conditions. For the unbounded flow case, the dependence of the present calculated results on the domain size is tested. Four domains with different sizes are tested: D1 ($24d \times 24d \times 12d$), D2 ($24d \times 30d \times 18d$), D3 ($40d \times 50d \times 30d$) and D4 ($100d \times 100d \times 100d$). Following Kim (2006), the domain size is defined as the distance from the sphere centre to the boundary in the y-direction (direction of the velocity gradient). The grid density around the sphere is the same for different domain sizes.

https://doi.org/10.1017/jfm.2026.11397 Published online by Cambridge University Press

			Lift		Torque	
Re	$Re\,Sr$	N_p	C_L	$\lvert\delta\rvert$ (%)	C_T	$\lvert\delta\rvert$ (%)
20	50	4	1.5485	1.29	0.9428	0.36
		7	1.5288		0.9462	
43.75	16.4	4	0.2547	0.22	0.1204	0.04
		7	0.2553		0.1204	
150	30	5	0.0145	0.88	0.0055	0.48
		7	0.0144		0.0054	

Table 1. Effects of the polynomial order N_p on lift and torque coefficients. Here, δ represents the relative error compared to the result of $N_p = 7$. For $Re = 20$, 43.75, 150, the corresponding values are $L = 6$, 1, 1 and $H = 12$, 4, 4, respectively.

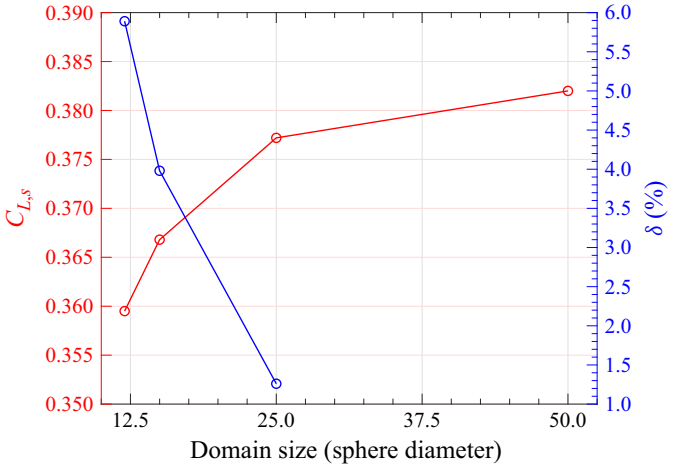


Figure 2. The shear-slip-induced lift coefficient and the relative difference versus the domain size at $Re = 5$, $Sr = 0.5$.

As mentioned by Kurose & Komori (1999), the boundary layer thickness around a translating sphere scales with $Re^{-0.5}$ in an unbounded environment, thus the largest domain size is needed for the lowest Reynolds number case. The convergence of the shear-slip-induced lift coefficient with increasing domain size is illustrated for $Re = 5$, $Sr = 0.5$ by the red curve in figure 2. The relative percentage difference δ compared to the result from the largest domain (D4) remains below 1.5 % once the domain size reaches $25d$ in the y-direction. To minimise the domain size influence, domain D3 is used for all subsequent simulations of unbounded linear shear flow.

3. Results and discussion

In this section, we propose the lift model for the unbounded linear shear flow, single-wall-bounded linear shear flow and plane Poiseuille flow, which are denoted as $C_{L,s}$, $C_{L,\,ws}$ and $C_{L,\,Poiseuille}$, respectively.

3.1. *Lift model for unbounded linear shear flow*

First, we revisit the classical problem of the lift force acting on a translating sphere in a simple shear flow. We focus on the moderate Reynolds number regime ($5 \leqslant Re \leqslant 20$) and $0.2 \leqslant Sr \leqslant 2.5$, and extend the existing model for a better prediction. The Saffman lift

https://doi.org/10.1017/jfm.2026.11397 Published online by Cambridge University Press

considering only the leading order can be expressed as

$$C_{L,s}^{Saffman} = \frac{18}{\pi^2} J_L \varepsilon, \tag{3.1}$$

with the conditions $\varepsilon = \sqrt{|Sr|\,/Re} \gg 1$, $Re \ll 1$ and $Re\,|Sr| \ll 1$. At $|Sr| \gg 1$, a second-order term $-11\,Sr/8$ becomes comparable to the first term and cannot be neglected. McLaughlin (1991) showed that the second term is also important at $\varepsilon \ll 1$, and results in a significant decrease of the lift force. Theoretical extension of the J_L function to arbitrary ε was done by Asmolov (1990) and McLaughlin (1991), and the explicit expression of $J_L(\varepsilon)$ in the limit of $\varepsilon \gg 1$ and $\varepsilon \ll 1$ is given by McLaughlin (1991). Based on the numerical integration results provided by McLaughlin (1991) for $0.1 \leqslant \varepsilon \leqslant 20$, Mei (1992) proposed the fitting function for J_L as

$$J_L^{Mei} = 0.6765\left\{1 + \tanh\left[2.5\,(\lg\varepsilon + 0.191)\right]\right\}\{0.667 + \tanh\left[6\,(\varepsilon - 0.32)\right]\}. \tag{3.2}$$

Note that 'lg' in the above equation denotes the base-10 logarithm, while 'ln' (used elsewhere) denotes the natural logarithm. However, the above extensions of the Saffman lift predict a negative lift for a small value of ε, which is opposite to the DNS results. Legendre & Magnaudet (1998) used their DNS data at $Sr = 0.2$ and 0.5 for $Re < 1$, and the theoretical results of McLaughlin (1991) for $\varepsilon > 0.8$, to propose their empirical expression as

$$J_L^{L\&M} = 2.255\left(1 + 0.2/\varepsilon^2\right)^{-1.5}, \tag{3.3}$$

which avoids the negative value and thus indicates a positive leading-order term for (3.1). The DNS work of Cherukat *et al.* (1999) showed that for low Reynolds numbers, the inclusion of the second-order term can improve the agreement between the model prediction and their DNS data. For relatively high Re (before the lift force changes its sign at $Re = 40-100$), a damping for the second term is added by Shi & Rzehak (2019) to avoid the negative lift, as follows:

$$C_{L,s}^{Shi} = \frac{18}{\pi^2} J_L \varepsilon - \frac{11}{8} Sr \exp\left(-0.5\,Re\right). \tag{3.4}$$

Although numerous DNS have been carried out to calculate the lift on a spherical particle in unbounded linear shear flow, the results deviate from each other significantly, especially when the magnitude of the lift coefficient is small, and few works have been devoted to $Sr > 1$. As discussed in the literature (Kim 2006; Homann, Bec & Grauer 2013), the deviation between different DNS results is probably due to the confinement effect of the computational domain. Our numerical data for the unbounded lift coefficients together with some of the above-mentioned lift models are plotted as a function of Sr for different Re in figure 3. The model by Legendre & Magnaudet (1998) is shown as a blue line by substituting the J_L function (3.3) to Saffman's first-order term (3.1). It predicts the lift at low Reynolds number and for low Sr at moderate Reynolds number well, while underestimating the lift for higher Sr. The finite Re model of Shi & Rzehak (2019) (3.4) using the J_L function (3.3) also underestimates the lift force, since the additional second term is negative. Thus a correction is proposed for J_L as

$$J_L^{Present} = 2.255\left(1 + 0.2/\varepsilon^2\right)^{-1.5\left\{1-\tanh\left[\ln(Re\,|Sr|)/2-1\right]\right\}/2}, \tag{3.5}$$

which recovers the original form of $J_L^{L\&M}$ (3.3) at a small shear Reynolds number $Re\,|Sr|$, and approaches $J_L^{Saffman}$ (3.4) with the increase of $Re\,|Sr|$. Our model agrees well with the

https://doi.org/10.1017/jfm.2026.11397 Published online by Cambridge University Press

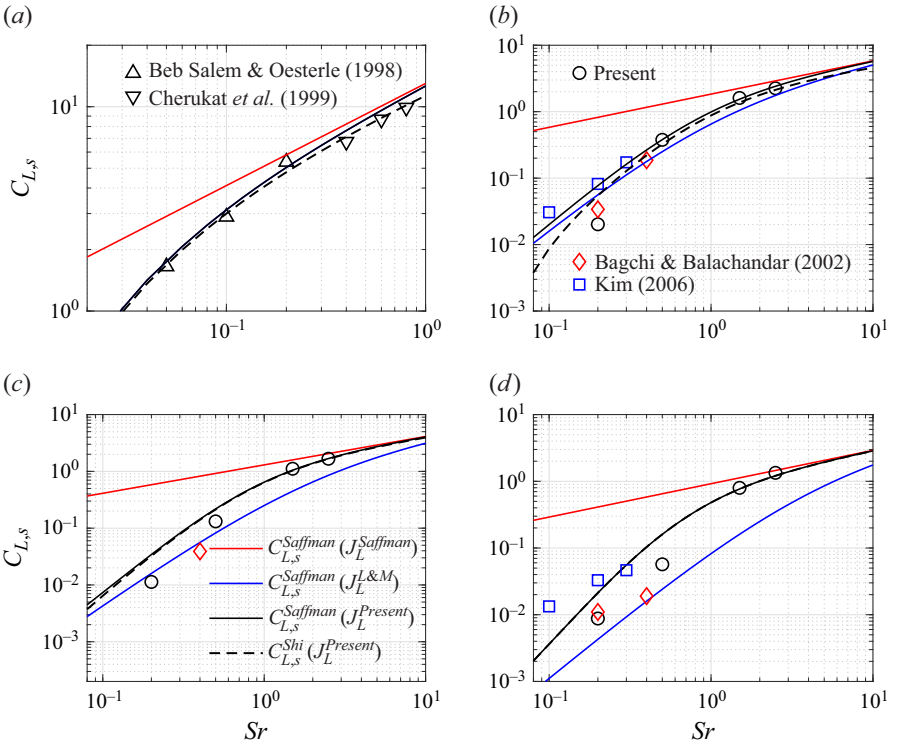


Figure 3. Lift coefficient for unbounded linear shear flow: (*a*) $Re = 0.1$, (*b*) $Re = 5$, (*c*) $Re = 10$, (*d*) $Re = 20$.

data from Ben Salem & Oesterle (1998) and Cherukat *et al.* (1999) at low Re for $Sr < 1$. The present model agrees well with the results of Kim (2006) for finite Re at low Sr. By applying the present J_L to model (3.4), as shown by the black dashed lines in figure 3, the new model is in better agreement with the present data and those given by Bagchi & Balachandar (2002) at $Re = 5$, while no distinctive difference occurs for other Reynolds numbers. Therefore, in the following, $C_{L,s}$ takes the form

$$C_{L,s2} = C_{L,s}^{Saffman}, \tag{3.6}$$

with $C_{L,s}^{Saffman}$ and J_L given by (3.1) and (3.5), respectively. It is interesting that the computed lift approaches the Saffman lift as Sr increases to a value that corresponds to ε being well below 1 for finite Reynolds numbers. Though the present model fits the data well, it should be used with caution, since the idea of modelling the lift at finite ε by employing the J_L function inside the leading-order term of the Saffman force is strictly valid only for low Reynolds numbers and $\varepsilon > 1$, as pointed out by Shi & Rzehak (2019).

There are typically three mechanisms to describe the lift force on a sphere. At low Reynolds numbers, there is a vorticity mechanism where the lift varies with the square of the maximal vorticity on the particle surface (Legendre & Magnaudet 1997). The vorticity mechanism is replaced by two other mechanisms for relatively high Reynolds numbers: the 'L' mechanism and the 'S' mechanism. The 'L' mechanism is related to the vorticity of the undisturbed flow, which results from the inviscid effect and exerts a lift force in the same direction as the low-Re Saffman lift (Lighthill 1956; Auton 1987). The 'S' mechanism is related to the surface vorticity, which is negligible for a clean spherical bubble with free-slip surface, but causes the decrease in the lift force

https://doi.org/10.1017/jfm.2026.11397 Published online by Cambridge University Press

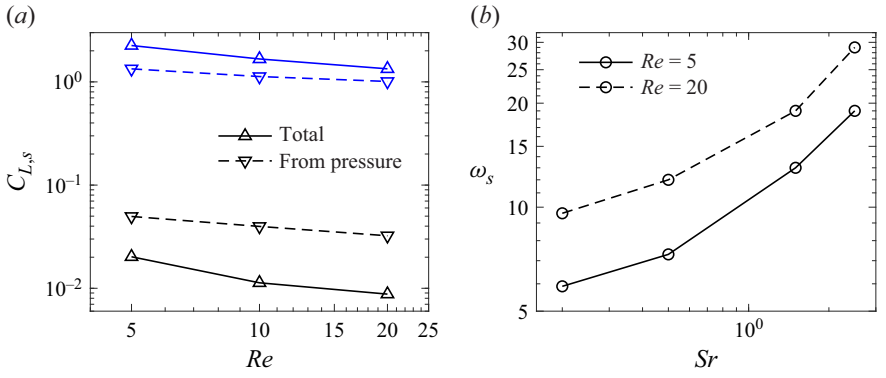


Figure 4. (*a*) The lift coefficient and the contribution from pressure for unbounded linear shear flow at $Sr = 0.2$ (black lines) and $Sr = 2.5$ (blue lines). (*b*) The variation of the maximal vorticity on the particle surface with Sr.

with increasing internal viscosity and even a negative lift at high particle Reynolds numbers (Adoua, Legendre & Magnaudet 2009; Shi, Climent & Legendre 2024). The lift coefficient and the contribution from pressure for unbounded linear shear flow at $Sr = 0.2$ and $Sr = 2.5$ are plotted in figure 4(*a*). One can see that the lift force decreases with increasing Reynolds number for both $Sr = 0.2$ and $Sr = 2.5$. Nevertheless, the lift coefficient for $Sr = 2.5$ is much larger than that for $Sr = 0.2$. This can be explained in two ways. The first is related to the 'L' mechanism: a larger Sr corresponds to a larger vorticity of the undisturbed flow and thereby a larger lift force resulted from the pressure contribution, as shown in figure 4(*a*). The second is related to the observation in figure 4(*a*) that the contribution of viscous force to the lift is negative for $Sr = 0.2$, whereas it becomes positive for $Sr = 2.5$. Shi *et al.* (2024) observed that the 'S' mechanism played a role for a droplet at $Sr = 0.2$ when the Reynolds number exceeds 5. Therefore, for the finite Reynolds number regime studied here (i.e. 5–20), the 'S' mechanism may be regarded as the reason for particularly low lift coefficient being close to zero for low Sr, whereas the 'L' mechanism causes a high lift coefficient being $O(1)$ for high Sr. The variations of the maximal vorticity on the particle surface with Sr for $Re = 5$ and 10 are compared in figure 4(*b*), and the trend of the variation is similar.

3.2. *Lift model for single-wall-bounded linear shear flow*

For a non-rotating particle translating in a single-wall-bounded linear shear flow, the Oseen and Saffman lengths are introduced as $l_u = \nu/|u_{slip}|$ and $l_g = \sqrt{\nu/|\dot{\gamma}|}$, respectively. The particle–wall separation distance normalised by the Oseen and Saffman lengths is represented as

$$L_U = l/l_u = Re\, L, \quad L_G = l/l_g = \sqrt{Re\,|Sr|}\, L. \tag{3.7}$$

The wall lies in the inner region when $\max\{L_U, L_G\} \ll 1$, and in the outer region when $\max\{L_U, L_G\} \gg 1$. In addition to the shear-slip-induced lift, there are another two kinds of lift forces in the wall-bounded case at low Reynolds numbers. The wall-slip-induced lift is caused by the interaction of the Stokeslet with the wall (Vasseur & Cox 1977; Takemura & Magnaudet 2003). The shear-wall-induced lift arising from the interaction between the stresslet and the inner-region wall is proportional to Sr^2 (Cherukat & Mclaughlin 1994; Magnaudet, Takagi & Legendre 2003). Thus for $Sr > O(1)$ with the wall lying in the inner region, the shear-wall-induced lift becomes non-negligible compared to the shear-slip-induced lift, which is proportional to Sr.

https://doi.org/10.1017/jfm.2026.11397 Published online by Cambridge University Press

The lift model for high Sr has been considered by Ekanayake *et al.* (2021), covering the ranges $2 \times 10^{-3} \leqslant Re \leqslant 2 \times 10^{-1}$ and $4 \times 10^{-3} \leqslant Re\,|Sr| \leqslant 4 \times 10^{-1}$, and $0.6 \leqslant L \leqslant 4.75$:

$$C_{L,ws}^{Ekanayake} = \frac{2}{\pi}\left(\frac{Sr^2}{4}C_{L,1} - \frac{Sr}{2}C_{L,2} + C_{L,3}\right), \tag{3.8}$$

with

$$C_{L,1} = \left[0.93\exp\left(-0.88\,Re\,|Sr|/4\right) - 0.03\exp\left(-1000\,Re\,|Sr|/4\right)\right] C_{outer} + \left(1 + \sqrt{Re\,|Sr|}/2\right) C_{inner}, \tag{3.9}$$

$$C_{outer} = 2.231\exp\left(-0.1054L_G^2 - 0.3859L_G\right), \tag{3.10}$$

$$C_{inner} = 1.0575/\,(2L) - 2.4007/(2L)^2 + 1.3174/(2L)^3, \tag{3.11}$$

$$C_{L,2} = -h_L\frac{9}{\pi}J_L\varepsilon\frac{2}{|Sr|} - 2.6729 - 0.8373/\,(2L) + 0.4683/(2L)^2, \tag{3.12}$$

$$C_{L,3} = \frac{18\pi}{32 + 2L_U + 3.8L_U^2 + 0.049L_U^3} + 0.4757/(2L) - 1.268/(2L)^2 + 0.683/(2L)^3, \tag{3.13}$$

where h_L takes the original form of Takemura *et al.* (2009) as

$$h_L^{Takemura} = 1 - \exp\left(-\frac{11}{96}\pi^2 L_G/J_L\right), \tag{3.14}$$

J_L is given in (3.3), and L_U and L_G are given in (3.7). Their model well captures the lift when the particle–wall separation distance lies between the inner and outer regions.

For higher Reynolds numbers, Shi *et al.* (2021) proposed the lift model for $0.1 \leqslant Re \leqslant 100$, $-0.5 \leqslant Sr \leqslant 0.5$ and $0.75 \leqslant L \leqslant 4$ as

$$C_{L,ws}^{Shi} = g_L^{Shi}C_{L,w}^{Shi} + h_L^{Shi}C_{L,s}^{Shi}, \tag{3.15}$$

where $C_{L,s}^{Shi}$ is given by the first term of (3.4), and

$$g_L^{Shi} = \mathrm{e}^{-0.22\varepsilon^{0.8}L_G^{2.5}\exp\left(-0.01\,Re^2\right)}, \tag{3.16}$$

$$h_L^{Shi} = 1 - \exp\left(-\frac{11}{96}\pi^2\frac{L_G}{J_L}\left(1 + 0.1771/L + 0.1608/L^2 - 0.035/L^3\right)\right), \tag{3.17}$$

$$C_{L,w}^{Shi} = C_{L,w0}^{\mathrm{T\&M}}\left[1 + \left(0.37\,Re - 0.12\,Re^{0.5}\right)\tanh\left(0.2\,Re\,L^2\right)\right]\left(\frac{2}{3}L\right)^{-2\tanh(0.01\,Re)}, \tag{3.18}$$

$$C_{L,w0}^{\mathrm{T\&M}} = \begin{cases} \frac{9}{8}\left[1 + 0.13L_U\,(L_U + 0.53)\right]^{-1} & \text{for} \quad L_U \leqslant 10, \\ 8.94L_U^{-2.09} & \text{for} \quad L_U > 10. \end{cases} \tag{3.19}$$

Their model has accounted for the nonlinear coupling of the wall-slip and shear-slip-induced lift force due to the finite Reynolds number effect. To propose a lift model for a finite Reynolds number with higher shear rate, we take the form given by Shi *et al.* (2021), with a correction term from the outer-region part of the shear-wall-induced lift model by Ekanayake *et al.* (2020), as follows:

$$C_{L,ws} = g_L C_{L,w} + h_L C_{L,s} + C_{L,Sr2}, \tag{3.20}$$

https://doi.org/10.1017/jfm.2026.11397 Published online by Cambridge University Press

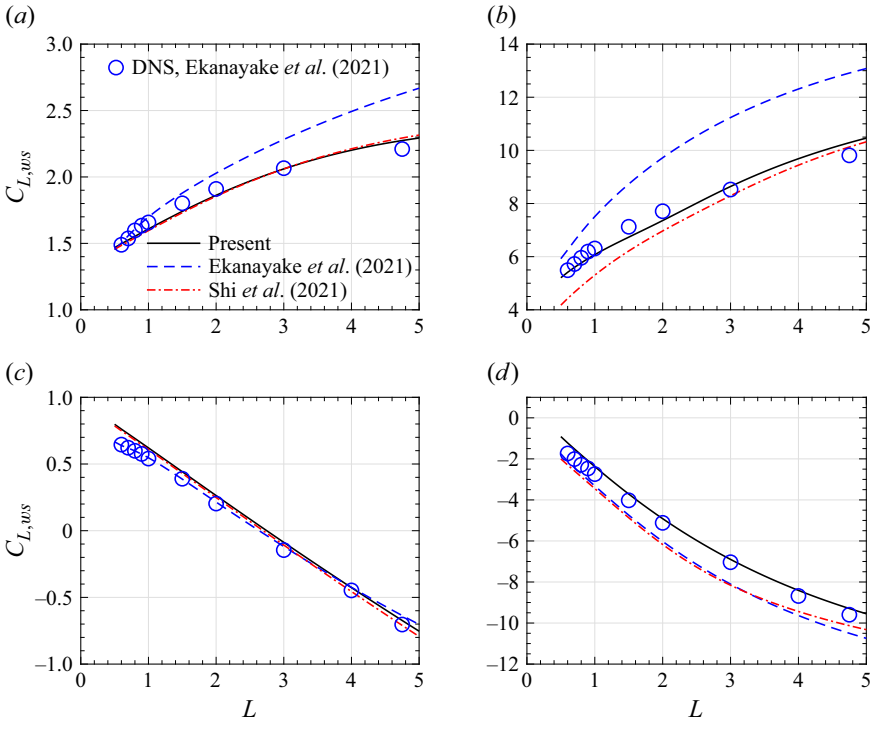


Figure 5. Lift coefficient for single-wall-bounded linear shear flow at $Re = 0.2$ and (*a*) $Sr = 0.2$, (*b*) $Sr = 2$, (*c*) $Sr = -0.2$, (*d*) $Sr = -2$.

where

$$C_{L,w} = C_{L,w}^{Shi}, \quad C_{L,s} = C_{L,s2}, \quad g_L = \left(g_L^{Shi}\right)^{1+\tanh(Sr)}, \quad h_L = h_L^{Shi}, \tag{3.21}$$

$$C_{L,Sr2} = \frac{Sr^2}{2\pi}\left[0.93\exp\left(-0.88\,Re\,|Sr|/4\right) - 0.03\exp\left(-1000\,Re\,|Sr|/4\right)\right] C_{outer}, \tag{3.22}$$

with $C_{L,w}^{Shi}$, $C_{L,s2}$, g_L^{Shi}, h_L^{Shi} and C_{outer} given by (3.18), (3.6), (3.16), (3.17) and (3.10), respectively.

The comparison between the data from Ekanayake *et al.* (2021) and the above models is shown in figure 5. The model of Ekanayake *et al.* (2021) fits the data better at small particle–wall separation distance at relative small Sr. Our model fits well with most of the data and gives better prediction for those near the outer region. At small Sr, our model approaches the model of Shi *et al.* (2021), which could consequently reduce to the outer-region shear-slip (wall-slip) lift model at low Reynolds numbers with the vanishing wall (shear) effect. Our model is promising for higher Sr since the Sr^2 term is included in our model.

Figure 6 shows the lift coefficients as functions of Reynolds number. Our numerical results are compared to the above-mentioned single-wall-bounded lift model for low Sr (3.15), and the unbounded lift models (3.1) and (3.6). As shown by the black lines in figure 6, the Sr^2 term is important for small L, especially for negative Sr when the shear-slip-induced lift and wall-slip-induced lift are in the opposite direction. Our model reduces to the model of Shi *et al.* (2021) as Sr approaches zero, which is in excellent agreement with our DNS results for $Sr \leqslant 0.5$. The present model for the unbounded case (3.6) gives a

https://doi.org/10.1017/jfm.2026.11397 Published online by Cambridge University Press

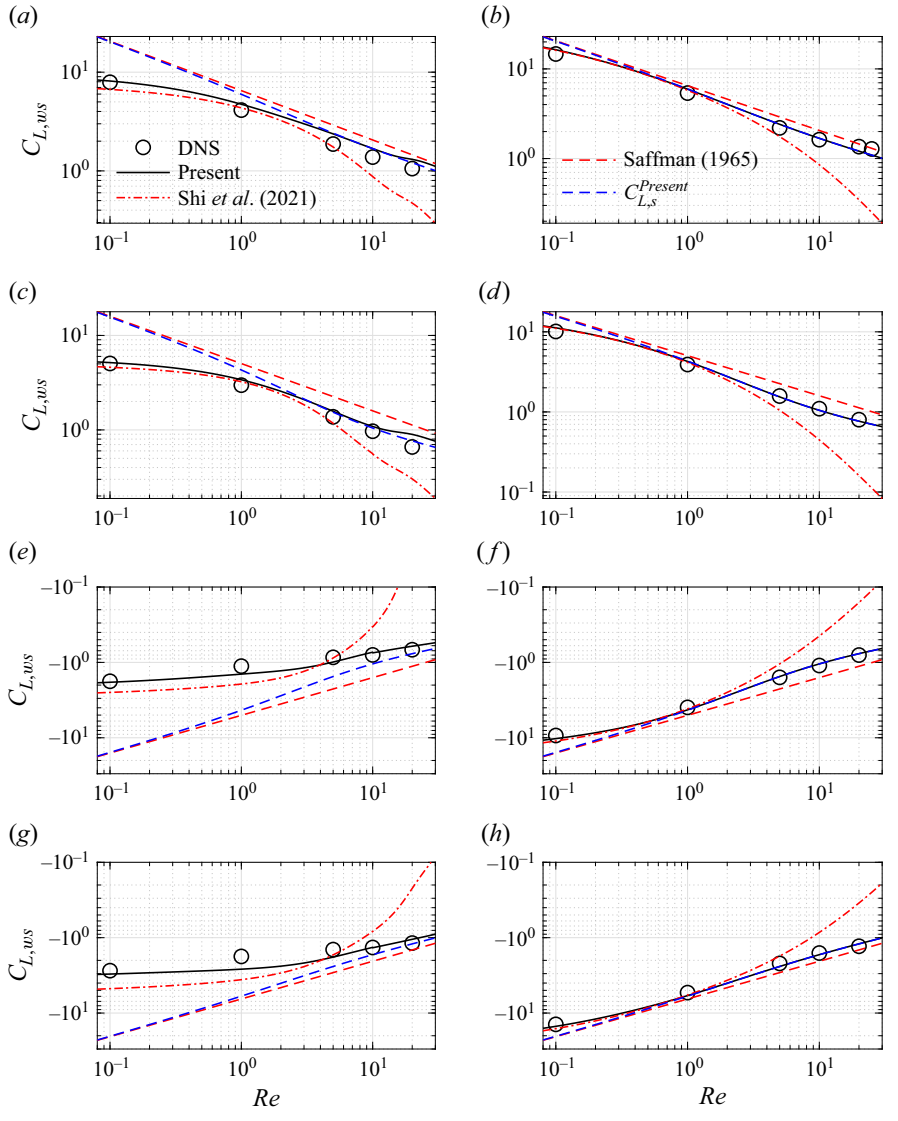


Figure 6. Lift coefficient for single-wall-bounded linear shear flow: (a,c,e,g) $L = 1$, (b,d,f,h) $L = 6$. Subplots from the top to the bottom correspond to $Sr = 2.5$, 1.5, -1.5, -2.5, respectively. The present model is given in (3.20).

better prediction for relatively high Reynolds numbers ($10 \leqslant Re \leqslant 20$). Our wall-bounded model converges to the unbounded shear flow model with increasing L or Re, which demonstrates that the wall effect becomes negligible.

3.3. *Lift model for plane Poiseuille flow*

For the case of Poiseuille background flow, the ratio of channel half-width to particle diameter H should be considered as the fourth dimensionless parameter. Here, we employ two ways to formulate the lift coefficient for the Poiseuille flow.

For the first approach, we utilise the model developed for Couette flow (Wang *et al.* 2025). The lift force for Poiseuille flow is obtained by correcting the lift for Couette flow

https://doi.org/10.1017/jfm.2026.11397 Published online by Cambridge University Press

as follows:

$$C_{L,Poiseuille} = C_{L,Couette} + C_{L,ps1}, \tag{3.23}$$

where $C_{L,Couette}$ is evaluated with the model proposed in our previous study (Wang *et al.* 2025).

For the second approach, inspired by the form of the single-wall-bounded lift model, the lift coefficient for Poiseuille flow is decomposed into

$$C_{L,Poiseuille} = g_L C_{L,w} + h_L C_{L,ps2} + C_{L,Sr2} + \Delta C_{L,w}, \tag{3.24}$$

where g_L, h_L, $C_{L,w}$ and $C_{L,Sr2}$ are given in (3.21) and (3.22), respectively. The shear-slip-induced lift term $C_{L,s}$ is replaced with $C_{L,ps2}$ to account for the effect of the parabolic shear. Here, $\Delta C_{L,w}$ is the correction term due to the far side wall, and its model is adopted from our previous study (Wang *et al.* 2025) as

$$\Delta C_{L,w} = -\exp(\alpha_w\, Re)\,(0.0373H + 1.1436)\left(\frac{L}{H}\right)^{0.2098H+1.2434}, \tag{3.25}$$

$$\alpha_w = -\frac{0.4245H^{0.2248H-0.67}}{L^{0.2248H+2.189}} - 0.4116H + 0.5725. \tag{3.26}$$

For both methods of lift decomposition, we ensure that $C_{L,Poiseuille}$ converges to the single-wall-bounded flow case with the increase of channel width.

3.3.1. *Modelling of $C_{L,ps1}$*

To facilitate the modelling, we model $C_{L,ps1}$ at positive and negative Sr separately. The parameter ranges considered are the same as for the Couette flow case (Wang *et al.* 2025), i.e. $0.1 \leqslant Re \leqslant 100$, $-0.5 \leqslant Sr \leqslant 0.5$, $1 \leqslant L \leqslant 6$, $4 \leqslant H \leqslant 12$. For positive Sr, as shown in figures 7(*a–f*), the correction of the lift force for the Poiseuille flow is negative for relatively low Re, and becomes positive when Re exceeds a critical value. From the present DNS data, the critical Reynolds number at which $C_{L,ps1}$ changes sign primarily depends on H, with the critical Reynolds number decreasing as H increases. The negative value at low Reynolds numbers indicates that when the fluid inertial effect is small, the curvature effect of the parabolic shear flow produces an addition lift opposite to the lift produced by the linear shear flow, which is more pronounced for larger L. It is reasonable that this part of the lift may overtake the positive part when the particle becomes neutrally buoyant, causing the two-way particle migration (Segré & Silberberg 1961).

At moderate Reynolds numbers, the positive $C_{L,ps1}$ has not been mentioned in any previous studies, to our knowledge, which induces a significant enhancement in the lift, especially when $C_{L,Couette}$ approaches 0 at $Re \sim O(10)$ and $L \geqslant 3$. Here, $C_{L,ps1}$ monotonically approaches 0 as Re further increases, and becomes negligibly small for $Re \geqslant 50$, except for the case $L = 3$ and $H = 4$ in figure 7(*d*), where the quadratic effect remains pronounced. We propose a correlation of $C_{L,ps1}$ for $Sr > 0$ as

$$\begin{aligned} C_{L,ps1} = {} & Sr^{1+(0.5-Sr)Re/H}\left(\frac{L}{H}\right)^{2+\tanh\left(0.067\,Sr\,10^{H-4}\right)\lg(Re)} \\ & \times\left\{\frac{-128H^{-1.53}}{Re+37.3H^{-1.78}}\left[1+(1.2-Sr)\exp(4-H)\left(1-\tanh(4L-7.6)\right)/2\right]+3\right\} \\ & \times\left\{1-\tanh\left[0.8\left(\ln(Re)+0.253(\ln H)^3-2.08(\ln H)^2+5.72\ln H-7.02\right)\right]\right\}. \end{aligned} \tag{3.27}$$

https://doi.org/10.1017/jfm.2026.11397 Published online by Cambridge University Press

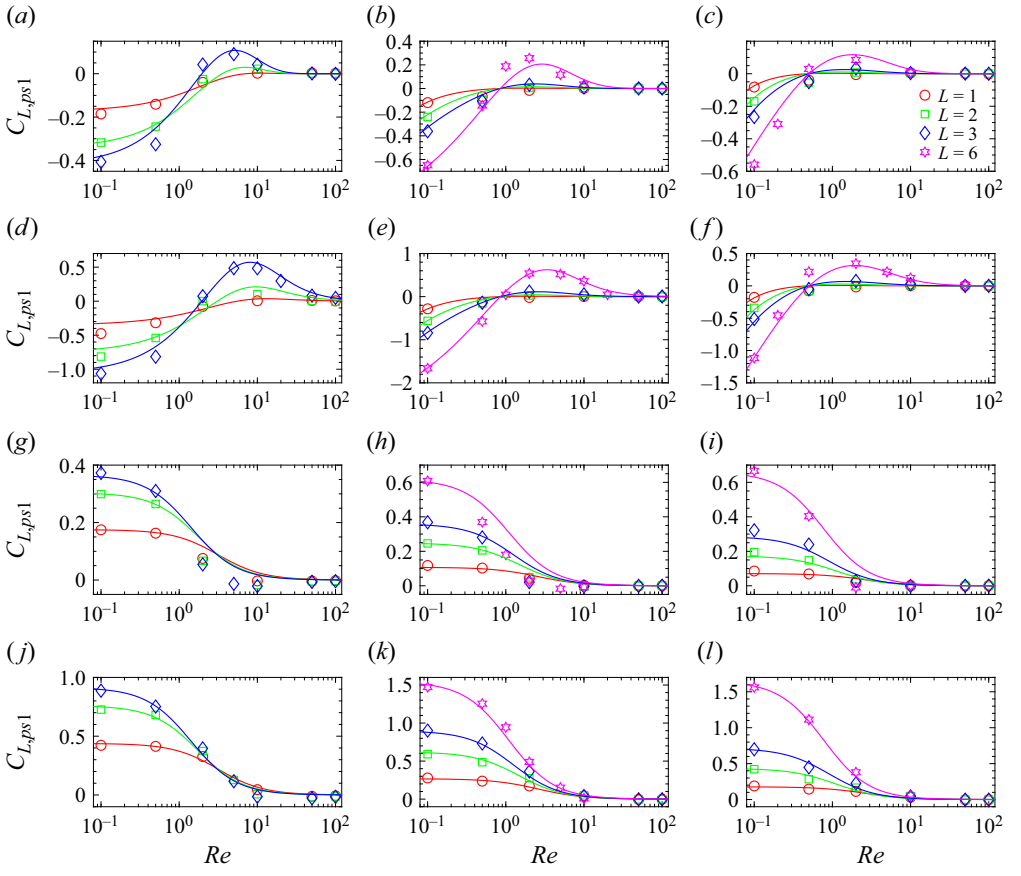


Figure 7. Lift coefficient correction term $C_{L,ps1}$ for the Poiseuille flow: (a,d,g,j) $H = 4$, (b,e,h,k) $H = 8$, (c,f,i,l) $H = 12$. Subplots from the top to the bottom correspond to $Sr = 0.2$, 0.5, −0.2, −0.5, respectively. The lines represent our model (3.27). Symbols and lines with the same colour correspond to the same L.

For $Sr < 0$, as shown in figures 7$(g$–$l)$, the way $C_{L,ps1}$ varies with Re is similar to the case $Sr > 0$ to some extent. Here, $C_{L,ps1}$ is always opposite to $C_{L,s}$, indicating that the effect from the parabolic shear tends to suppress the linear-shear-induced lift at low Reynolds numbers, irrespective of the sign of Sr. For moderate Reynolds numbers, in contrast to $Sr > 0$, there scarcely exists a change of sign for most cases, and the magnitude of $C_{L,ps1}$ monotonically decreases to 0 as Re increases. Here, we propose the model of $C_{L,ps1}$ for $Sr < 0$ as

$$C_{L,ps1} = Sr\left[a_a\left(\frac{L}{H}\right)^{b_a} + c_a\right] \Big/ \left\{\exp\left[a_b\left(\frac{L}{H}\right)^{b_b} + c_b\right] Re^{1.5} + 1\right\}, \tag{3.28}$$

$$a_a = 44.3H^{-0.5471} - 18.97, \quad b_a = 2.526H^{0.3053} - 4.215, \tag{3.29}$$

$$c_a = -2149/H^3 + 621.4/H^2 - 36.24/H, \tag{3.30}$$

$$a_b = -7.907H^{-2.119}, \quad b_b = -0.06425H - 0.7797, \tag{3.31}$$

$$c_b = 0.01678H^2 - 0.2107H + 0.6111. \tag{3.32}$$

The lift force for the Poiseuille flow can now be calculated from (3.23). As shown in figure 8, for small H, $C_{L,Poiseuille}$ varies slowly at small Re. The present model is in good

https://doi.org/10.1017/jfm.2026.11397 Published online by Cambridge University Press

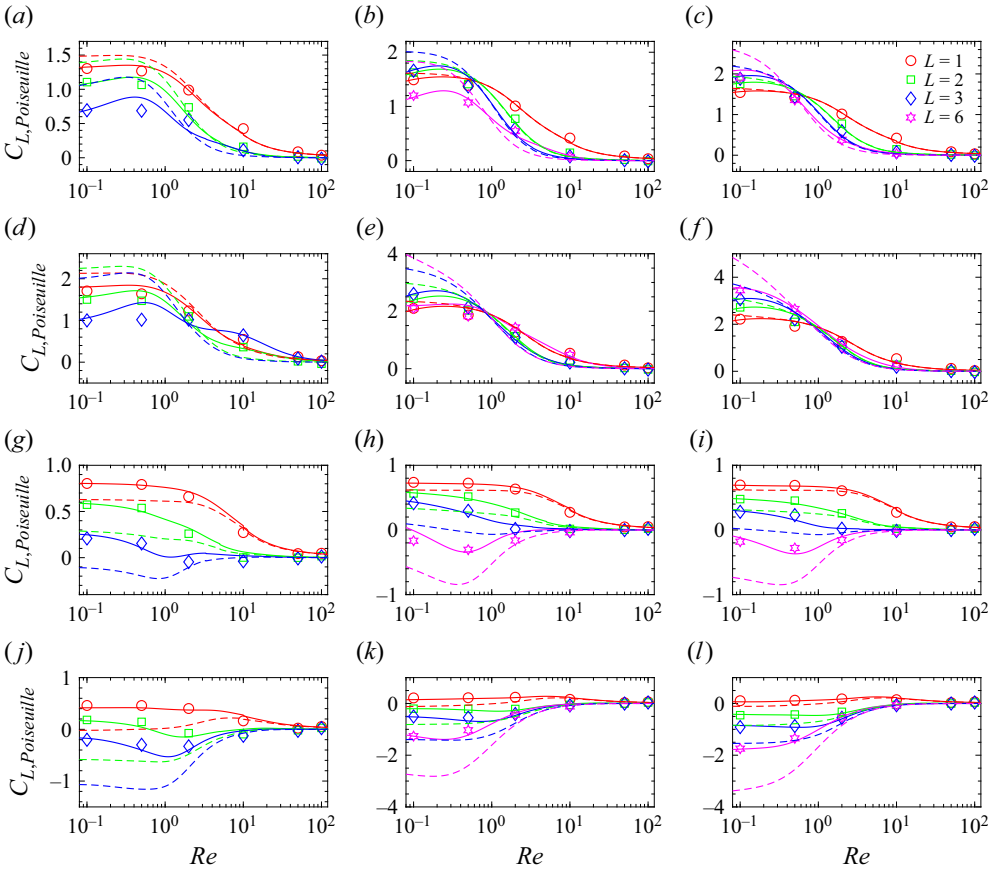


Figure 8. Lift coefficients for the Poiseuille flow, obtained from the correction of the lift coefficient for the Couette flow: (*a,d,g,j*) $H = 4$, (*b,e,h,k*) $H = 8$, (*c,f,i,l*) $H = 12$. Subplots from the top to the bottom correspond to $Sr = 0.2, 0.5, -0.2, -0.5$, respectively. Solid and dashed lines correspond to the present model (3.23) and the model for the Couette flow (Wang *et al.* 2025). Symbols and lines with the same colour correspond to the same L.

agreement with the DNS data. At low Re, the maximum relative difference between the lifts for the Poiseuille and Couette (dashed lines) flows is approximately 50 % for positive Sr, and even larger for negative Sr, in which case the direction of the lift may be different for two flows, as shown in figures 8(*g,j*).

3.3.2. *Modelling of* $C_{L,ps2}$

Here, we first propose the lift model for the unbounded Poiseuille flow based on the low Reynolds number theoretical results. Asmolov (1999) theoretically solved the problem for a large channel Reynolds number by the method of matched asymptotic expansion. The problem is considered as 'unbounded' when the wall effect is negligible and the lift was obtained by numerical integration. The lift coefficient for unbounded parabolic flow could take the form

$$C_{L,ps2} = \frac{18}{\pi^2} J_{L,ps} \varepsilon, \tag{3.33}$$

https://doi.org/10.1017/jfm.2026.11397 Published online by Cambridge University Press

where $J_{L,ps}$ is fitted based on the results by Asmolov (1999) as

$$J_{L,ps} = 2.255\left(1+\sigma^{0.9}/0.8\right)^{-1}\left[1+0.2\left(\mathrm{sgn}(u_{slip})\,\varepsilon^{-1}-1.7\sigma^{0.6}\right)^2\right]^{-2/(1+2\sigma)}. \quad (3.34)$$

In our simulations, the particle is always located in the lower half-channel, thus $\mathrm{sgn}(u_{slip}) = \mathrm{sgn}(Sr)$. Here, σ is given by

$$\sigma = \left(2\,(H-L)\sqrt{Re\,|Sr|}\right)^{-1}, \quad (3.35)$$

and $J_{L,ps}$ reduces to the form for linear shear when $(H-L)$ or $Re\,|Sr|$ is large, corresponding to small curvature or the large Reynolds number limit.

Then we consider the second way of modelling, as given by (3.24). Compared to the first way, here we focus on relatively lower slip velocities and a wider range of shear rates as $0.1 \leqslant Re \leqslant 20$ and $-2.5 \leqslant Sr \leqslant 2.5$. Since small particles are more widely encountered in engineering applications, the minimum width of the channel $H = 8$ is considered here.

Assuming that the shear effect and the wall effect are coupled in a similar way as in the linear shear case, we can obtain the the lift model for the Poiseuille flow by substituting (3.33) into (3.24). The present model is plotted as solid lines in figure 9, compared with the present data and the single-wall-bounded linear shear model (3.20). Here, $C_{L,ws}$ provides good predictions for moderate Reynolds numbers, while for low Reynolds numbers, $C_{L,ws}$ fails to reproduce the lift reduction as L increases to 6 for $H = 8$ and $Sr > 0$. This discrepancy arises not only from the confinement effect of the second wall but primarily from the non-negligible negative quadratic-shear-induced lift. Though the second model here does not give predictions of lift as precise as in the first model within the parameter space that we explored, it captures most of the lift coefficients well. The second model takes advantage of its simplicity and promising capability to capture the lift over a wider range of L and Sg, which benefits from its semi-empirical essence. With the increase of H, $1/L$, Re, Sr, $C_{L,Poiseuille}$ converges to $C_{L,ws}$. Further adjustments could be made by considering the interaction of the shear effect and wall effect more precisely.

3.4. *Lift and torque from rotation*

The rotation-induced lift is calculated by subtracting the lift on a non-rotating particle from the lift when the particle is forced to rotate. For linear shear flow, it has been recognised that $C_{L,\Omega}$ is proportional to the particle rotation rate, while being independent of the fluid shear rate in a wide range of Re and Rr (Kurose & Komori 1999; Bagchi & Balachandar 2002; Wang *et al.* 2025). For the Couette flow, the far side wall was found to have negligible effects on $C_{L,\Omega}$, while the near side wall effect was taken into consideration by our previous model (Wang *et al.* 2025), in the form

$$C_{L,\Omega}^{ws} = \left[\left(\frac{-1}{0.29+2.9L}+0.55\right)\mathrm{e}^{(0.1L^{-2.1}-0.16)\,Re}+0.45\,\mathrm{e}^{0.0032\,Re}\right]Rr. \quad (3.36)$$

For the Poiseuille flow, figure 10 shows the variation of the rotation-induced lift coefficient with Sg, which is the non-dimensional curvature of the velocity profile (i.e. the gradient of the fluid shear rate in the wall-normal direction) and is represented as

$$Sg = \frac{\partial^2 u_f}{\partial y^2}\frac{d^2}{u_{slip}} = \begin{cases} -\dfrac{Sr}{H-L} & (L<H)\quad \text{Poiseuille,} \\ 0 & \text{Couette.} \end{cases} \quad (3.37)$$

https://doi.org/10.1017/jfm.2026.11397 Published online by Cambridge University Press

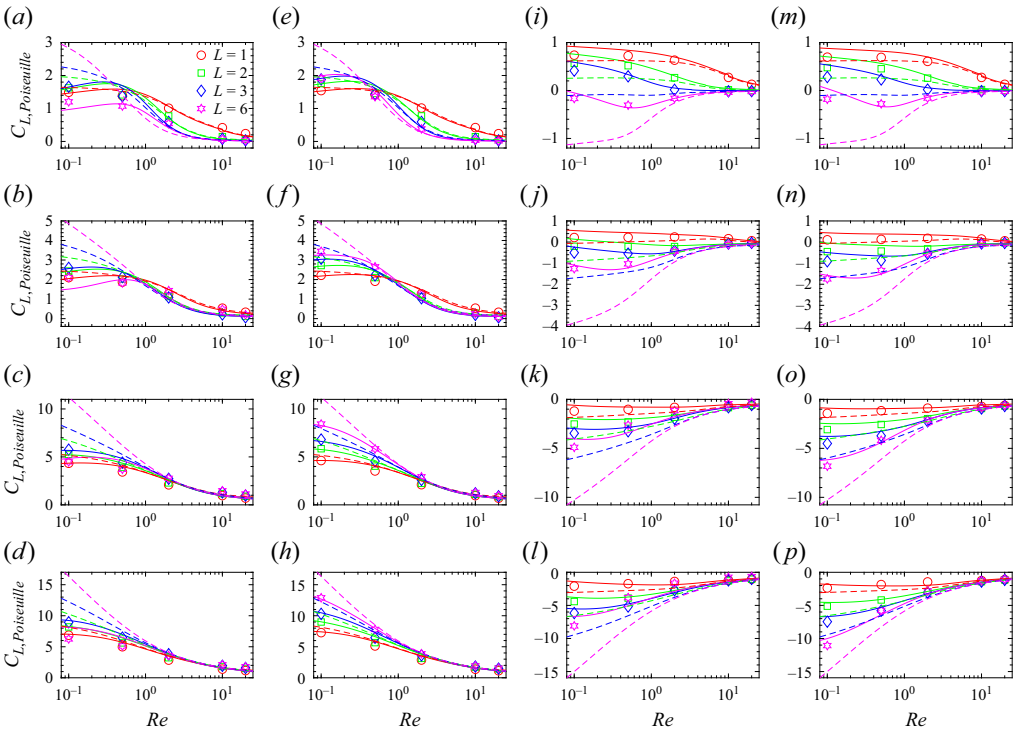


Figure 9. Lift coefficients for the Poiseuille flow: (*a–d*) $Sr = 0.2, 0.5, 1.5, 2.5$ with $H = 8$; (*e–h*) $Sr = 0.2, 0.5, 1.5, 2.5$ with $H = 12$; (*i–l*) $Sr = -0.2, -0.5, -1.5, -2.5$ with $H = 8$; (*m–p*) $Sr = -0.2, -0.5, -1.5, -2.5$ with $H = 12$, respectively. Solid and dashed lines correspond to the present model for $C_{L,Poiseuille}$ (3.24) and $C_{L,ws}$ (3.20). Symbols and lines of the same colour correspond to the same L.

The rotation-induced lift for the Poiseuille flow ($C^{ps}_{L,\Omega}$) approaches the value for the Couette flow ($C^{ws}_{L,\Omega}$) as $|Sg|$ decreases. Note that the zero value of Sg is only strictly reached when the sphere is in the Couette flow. In figure 10, the straight lines can approximately fit the data points at different Sg, especially for low Reynolds numbers. The slope decreases with increasing Re, while it increases with increasing L, indicating that the rotation-induced lift for the Poiseuille flow $C^{ps}_{L,\Omega}$ becomes more sensitive to the curvature when the particle is located closer to the channel centre. Based on these observations and the results in figure 10, we propose a correlation for the rotation-induced lift coefficient for the Poiseuille flow as

$$C^{ps}_{L,\Omega} = \left[0.143\, Re^{-0.282} L - 0.045\, Re^{-0.78} + 0.2/\left(1 + Re^2\right)\right] Sg\, Rr + C^{ws}_{L,\Omega}. \quad (3.38)$$

It should be noted that in our simulations the particle is always located in the lower half-channel where the fluid shear rate is positive, and positive Sr means lagging particle defined as positive slip velocity, and negative Sr means leading particle defined as negative slip velocity. Thus both Saffman-type (shear-slip-induced) lift force and the Magnus force on the clockwise-rotating (same rotation direction as the local fluid) particle point to the channel centre (i.e. positive lift) for positive Sr, and point to the near wall (i.e. negative lift) for negative Sr. In figure 10, Sg is varied by changing Sr, being positive for negative Sr, and negative for positive Sr from the definition (3.37). The rotation of the particle is always clockwise, then the dimensionless particle rotational velocity Rr is negative for positive Sg, which corresponds to negative Sr and negative slip velocity, and is positive for negative

https://doi.org/10.1017/jfm.2026.11397 Published online by Cambridge University Press

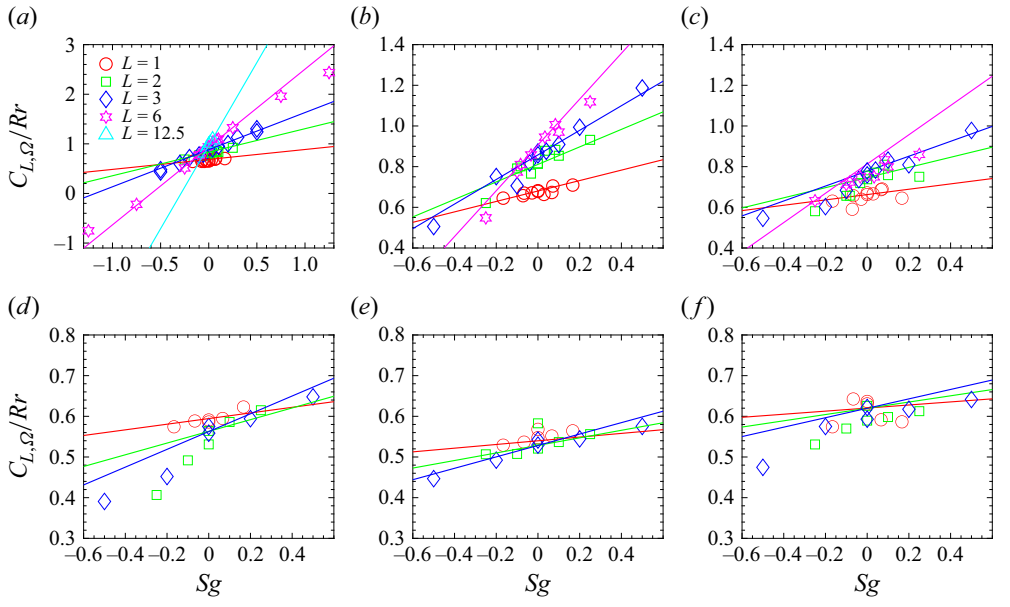


Figure 10. The rotation-induced lift coefficient normalised with Rr (-0.1 to 0.2) for $H = 4-25$ at (*a*) $Re = 0.1$, (*b*) $Re = 0.5$, (*c*) $Re = 2$, (*d*) $Re = 10$, (*e*) $Re = 50$, (*f*) $Re = 100$. The lines represent the model (3.38). Symbols and lines of the same colour correspond to the same L.

Sg, which corresponds to positive Sr and positive slip velocity. For $Sg > 0$, both the lift and Rr are negative, thus their ratio is positive. From figure 10, the effect of a positive (negative) Sg is to exert an additional force pointing to the same (opposite) direction as predicted by the Magnus effect. Consequently, the predicted rotation-induced lift force changes sign when Sg is below a certain negative value (only in the case $Sg < 0$ for a lagging particle). Thus unlike the inverse Magnus effect, which is associated with the turbulence transition of the boundary layer on the advancing side (Kray, Franke & Frank 2005; Muto, Tsubokura & Oshima 2012; Kim *et al.* 2014), we observe that an inverse Magnus effect occurs at a low Reynolds number, as shown in figure 10(*a*) for $Re = 0.1$ and $L = 6$.

Then we attempt to investigate the reason for the direction change of the rotation-induced lift. The rotation-induced local viscous stress and pressure coefficients are defined as the non-dimensional viscous stress and pressure difference between rotating and non-rotating sphere in the y-direction:

$$C_{f,\Omega} = \left.\frac{\boldsymbol{n}\cdot\boldsymbol{\tau}\cdot\boldsymbol{e_y}}{\rho u_{slip}^2}\right|_{\Omega_z\neq 0} - \left.\frac{\boldsymbol{n}\cdot\boldsymbol{\tau}\cdot\boldsymbol{e_y}}{\rho u_{slip}^2}\right|_{\Omega_z=0}, \quad C_{p,\Omega} = \left.\frac{-p\boldsymbol{n}\cdot\boldsymbol{e_y}}{\rho u_{slip}^2}\right|_{\Omega_z\neq 0} - \left.\frac{-p\boldsymbol{n}\cdot\boldsymbol{e_y}}{\rho u_{slip}^2}\right|_{\Omega_z=0}. \tag{3.39}$$

To examine the effect of the parabolic shear on the lift force, we calculate the difference in the local rotation-induced stress coefficients between the Poiseuille and Couette flows. The surface contours of viscous stress difference ($\Delta C_{f,\Omega}$) and pressure difference ($\Delta C_{p,\Omega}$) seen from the positive z-axis (i.e. spanwise) direction are shown in figure 11. For $Re = 0.1$ and $Sr = 0.5$, the Magnus force points to the channel centre. From figures 11(*a*,*c*) for this case, it is the viscous stress that produces the negative lift (pointing to the near wall) and leads to an inverse Magnus force at a relatively large magnitude of Sg. For $Re = 100$ and $Sr = -0.5$, the Magnus force points to the channel wall. From figures 11(*b*,*d*) for this

https://doi.org/10.1017/jfm.2026.11397 Published online by Cambridge University Press

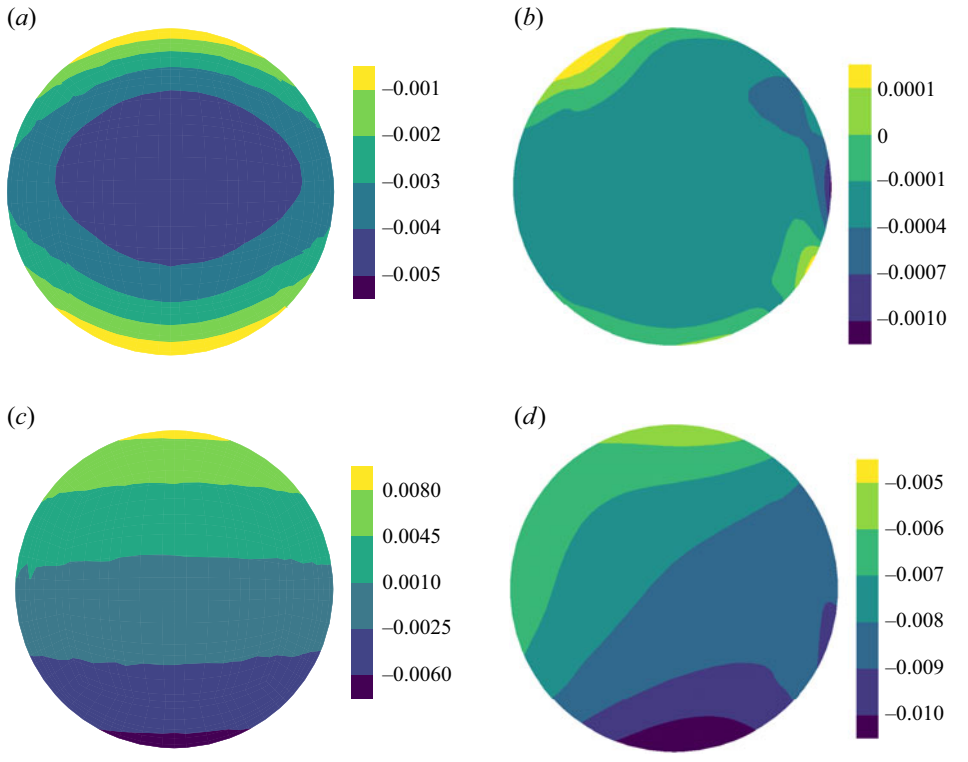


Figure 11. Surface contours showing the differences in the y-component of the rotation-induced viscous stress and pressure coefficients between Couette and Poiseuille flow configurations at $L = 3$, $H = 4$, seen from the positive z-axis (i.e. spanwise) direction. Viscous stress coefficient difference $\Delta C_{f,\Omega}$ at (*a*) $Re = 0.1$, $Sr = 0.5$, $Rr = 0.1$, and (*b*) $Re = 100$, $Sr = -0.5$, $Rr = -0.1$; pressure coefficient difference $\Delta C_{p,\Omega}$ at (*c*) $Re = 0.1$, $Sr = 0.5$, $Rr = 0.1$, and (*d*) $Re = 100$, $Sr = -0.5$, $Rr = -0.1$.

case, it is the pressure that produces the negative lift (pointing to the near wall) to enhance the Magnus lift.

We have shown that the rotation-induced lift can be opposite to the Magnus force for a lagging particle in Poiseuille flow. However, it is not clear whether the total lift force can be opposite to the Magnus force. Figure 12 shows the linear variation of lift and torque coefficients with Rr for both Couette and Poiseuille flows in a wide range of Rr at $Re = 0.1$. The direction of the rotation-induced lift force is altered by the curvature effect of the velocity profile. At $Rr = 10$, the rotation-induced lift exceeds the shear-slip-induced lift on a non-rotating particle, resulting in a total lift force with direction opposite to that of Magnus force. The torques for two flows have no discernible difference at low Re, and the equilibrium state of torque-free rotation is achieved approximately at $Rr = 1.25$.

The lift is dependent on the particle rotational velocity, which depends on the torque on the particle. Therefore, the model for the torque is needed for the application of the lift model to a rotating particle. The torque coefficient for a rotating particle can be modelled as

$$C_T = \left(Rr_{eq} - Rr\right) f_T, \tag{3.40}$$

where Rr_{eq} is the non-dimensional particle rotational velocity at the torque-free equilibrium state, and f_T is a torque factor. For low Sr ($\leqslant 0.5$), Shi *et al.* (2021) modified the model of Bagchi & Balachandar (2002) for the unbounded linear shear flow to account

https://doi.org/10.1017/jfm.2026.11397 Published online by Cambridge University Press

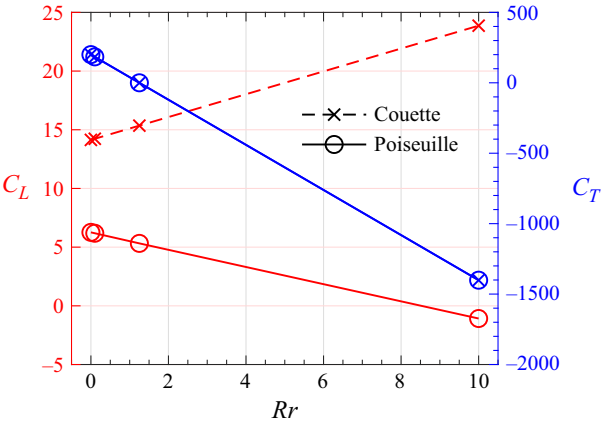


Figure 12. The total lift and torque coefficients versus the non-dimensional rotation rate at $Re = 0.1$, $Sr = 2.5$, $L = 6$ and $H = 8$.

for the influence of the nearby wall, while the wall effect is insignificant when the particle–wall separation distance is greater than one particle diameter. We propose a new model for the wall-bounded linear shear flow based on their models and our DNS data, as

$$Rr_{eq,ws} = Rr^{ls}_{eq,ws}\left(1 + 0.015\tanh\left(0.2\,Re\right)|Sr|^{2.2}\right), \tag{3.41}$$

with

$$Rr^{ls}_{eq,ws} = \begin{cases} Rr^{Shi}_{eq,ws}, & L \leqslant 1, \\ Rr^{B\&B}_{eq,ws}, & L > 1, \end{cases} \tag{3.42}$$

where

$$Rr^{Shi}_{eq,ws} = -\frac{C_{L,w0}}{96L^4}\left(1 - \frac{3}{16L} + \frac{9}{80L^3}\right) + \frac{Sr}{2}\left\{f_\Omega + \frac{1}{32L^4}\tanh\left(\frac{Re}{2}\right)\left[1 + \mathrm{sgn}\left(Sr\right)\right]\right\}\left\{1 - \frac{5}{128L^3}\,\mathrm{e}^{-Re/2}\right\} \tag{3.43}$$

and

$$Rr^{B\&B}_{eq,ws} = \frac{Sr}{2}f_\Omega, \tag{3.44}$$

with

$$f_\Omega = \begin{cases} 1 - 0.0364\,Re^{0.95}, & 0.5 \leqslant Re \leqslant 5, \\ 1 - 0.0755\,Re^{0.455}, & 5 < Re. \end{cases} \tag{3.45}$$

From figure 13, the model of Bagchi & Balachandar (2002) is in good agreement with our DNS data. However, it treats $Rr_{eq,\,ws}$ as a linear function of Sr, and appears to underestimate the free rotation rate at relatively high Sr and Re, as shown in figure 13(*b*). Thus a correction is made to the models of Bagchi & Balachandar (2002) and Shi *et al.* (2021) to obtain our model (3.41), which captures the nonlinear increase of $Rr_{eq,\,ws}$ with Sr, as shown in figure 13.

Then, based on our DNS data, we obtain a new model for the free rotation rate for a particle in the Poiseuille flow by modifying the model for the wall-bounded linear

https://doi.org/10.1017/jfm.2026.11397 Published online by Cambridge University Press

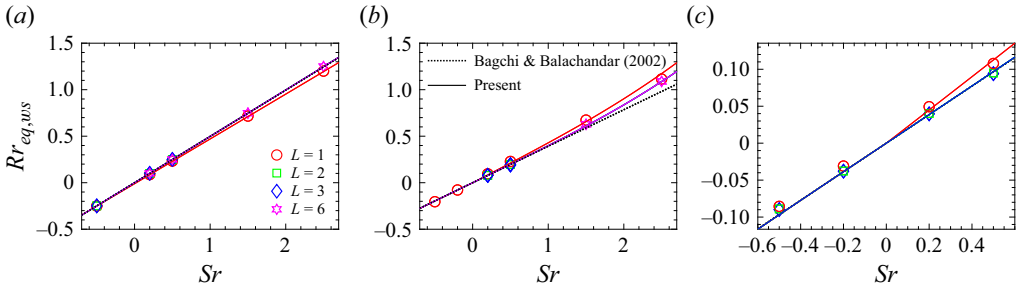


Figure 13. The non-dimensional free rotation rate for wall-bounded linear shear flow at (*a*) $Re = 0.1$, (*b*) $Re = 10$, (*c*) $Re = 100$. The present model is (3.41). Symbols and lines of the same colour correspond to the same L.

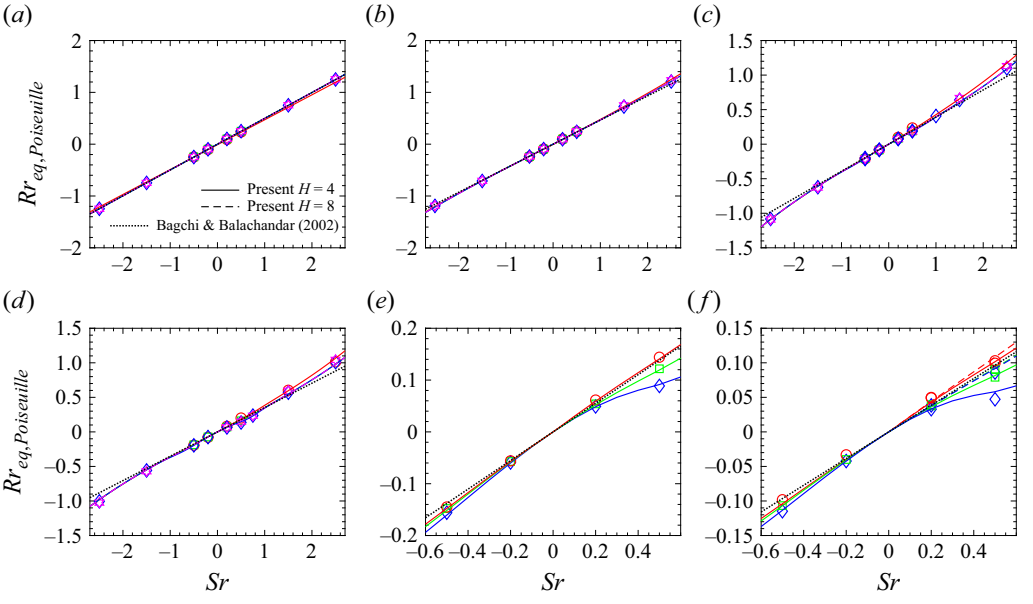


Figure 14. The non-dimensional rotation rate for Poiseuille flow at (*a*) $Re = 0.1$, (*b*) $Re = 2$, (*c*) $Re = 10$, (*d*) $Re = 20$, (*e*) $Re = 50$, (*f*) $Re = 100$. Symbols and lines of the same colour correspond to the same L as in figure 13.

shear flow:

$$Rr_{eq,Poiseuille} = Rr_{eq,ws}\,(1.3 - 0.3\exp(-Sg\,[\tanh(\ln(Re) - 3) + 1]\,[1 - \tanh(4\,|Sr| - 3)]\,/2))\,. \tag{3.46}$$

As shown in figure 14, the free rotation rate model proposed by Bagchi & Balachandar (2002) for linear shear flow well captures the free rotation rate for the Poiseuille flow at low Reynolds numbers, whereas our model is able to predict the nonlinear variation of the free rotation rate at relatively high Re and Sr.

Regarding the lift factor f_T, we employ the same model as for the Couette flow proposed in our previous study (Wang *et al.* 2025), which is a function of Re and L as

$$f_T = \frac{16}{Re}\left(1 + \frac{5}{128L^3} + \mathrm{e}^{-5.4\,Re^{-0.3}}\right). \tag{3.47}$$

https://doi.org/10.1017/jfm.2026.11397 Published online by Cambridge University Press

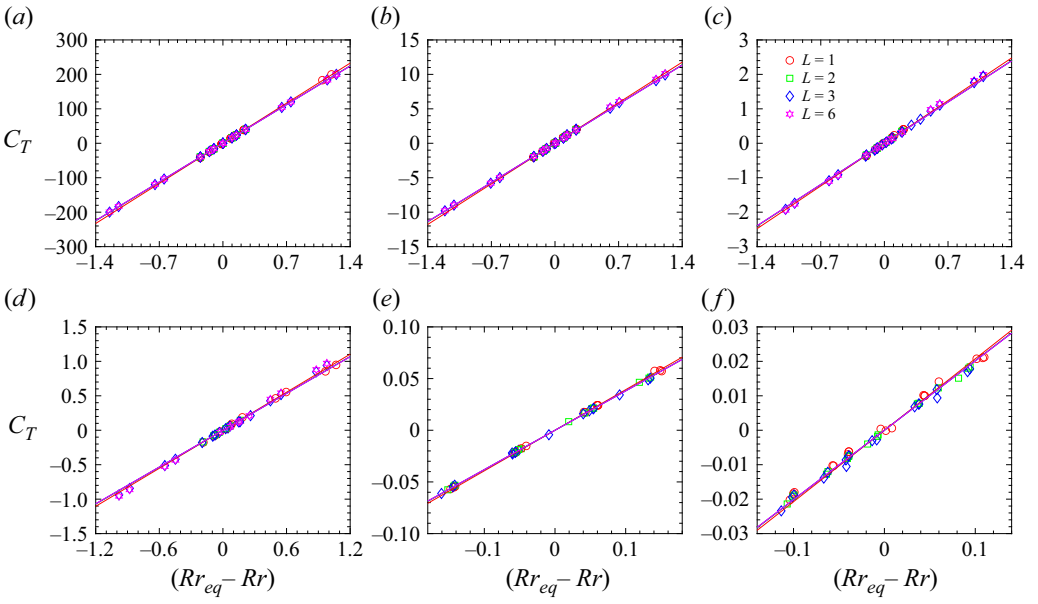


Figure 15. The torque coefficients for (*a*) $Re = 0.1$, (*b*) $Re = 0.5$, (*c*) $Re = 2$, (*d*) $Re = 10$, (*e*) $Re = 50$, (*f*) $Re = 100$. Symbols represent DNS data, and the lines represent our model (3.40), (3.46) and (3.47). Symbols and lines of the same colour correspond to the same L.

As shown in figure 15, the torque coefficients at different L almost collapse into a single line, and are well predicted by the present model (3.40), (3.46) and (3.47).

4. Conclusions

The lift and torque models for a spherical particle immersed in the linear and parabolic shear flows are proposed based on DNS results, covering the range of slip Reynolds number $0.1 \leqslant Re \leqslant 100$, non-dimensional shear rate $-2.5 \leqslant Sr \leqslant 2.5$, non-dimensional rotation rate $-0.1 \leqslant Rr \leqslant 0.2$, non-dimensional separation distance between particle and near side wall $1 \leqslant L \leqslant 6$, and non-dimensional channel half-width $4 \leqslant H \leqslant 25$.

The main results are summarised as follows.

(i) For a non-rotating particle in unbounded linear shear flow, a lift model (3.6) is proposed to extend the existing models (Saffman 1965; Legendre & Magnaudet 1998) to $Sr = -2.5$ to 2.5 at finite Reynolds numbers ($5 \leqslant Re \leqslant 20$).

(ii) A lift model for a non-rotating particle for single-wall-bounded linear shear flow (3.20) is proposed to extend the model given by Shi *et al.* (2021) to higher shear rate ($|Sr| \leqslant 2.5$) with the inclusion of the Sr^2 term from Ekanayake *et al.* (2021). The present model is an outer-region model and is valid for $0.1 \leqslant Re \leqslant 20$. Our model converges to the unbounded shear-slip-induced lift ($C_{L,s2}$ in (3.6)) as L increases, and to the single-wall-bounded lift ($C_{L,ws}^{Shi}$ in (3.18)) given by Shi *et al.* (2021) as Sr decreases.

(iii) For a non-rotating particle in the Poiseuille flow, two correlations (3.23) and (3.24) are proposed for the first time to account for the effects of the parabolic shear at finite slip Reynolds numbers. The first model is based on the correction of the lift model for the Couette flow and the simulation results for relatively low shear rates ($-0.5 \leqslant Sr \leqslant 0.5$). Based on the results tabulated by Asmolov (1999), the shear-slip lift model

https://doi.org/10.1017/jfm.2026.11397 Published online by Cambridge University Press

for unbounded parabolic flow is proposed as (3.33). The single-wall-bounded linear shear flow lift model and unbounded parabolic flow lift model are then utilised to obtain the second model for Poiseuille flow, which is applicable for a relatively wide range of shear rates ($-2.5 \leqslant Sr \leqslant 2.5$).

(iv) A rotation-induced lift model for a rotating particle in the Poiseuille flow is proposed in (3.38), which shows the lift enhancement for the leading particle ($Sr < 0$) and the lift attenuation for the lagging particle ($Sr > 0$) due to the curvature effect of the velocity profile, compared to the linear shear case. It is shown that the lift attenuation for the lagging particle ($Sr > 0$) at low Re is caused by the viscous stress, while the lift enhancement for the leading particle ($Sr < 0$) at high Re is caused by the pressure. An inverse Magnus force is observed for the lagging particle in Poiseuille flow at low Re, and even a total lift force with the direction opposite to both Saffman-type (shear-slip-induced) and Magnus (rotation-induced) forces is observed when the particle rotation rate is sufficiently large.

(v) Models for the free rotation rate of a particle immersed in the linear (3.41) and parabolic shear flows (3.46) are proposed, respectively. The torque coefficient model is then obtained with (3.40), (3.46) and (3.47).

For the parameter range studied, the highest channel Reynolds number is 14 400, which should lead to a turbulent flow. However, we observe a steady-state laminar flow in our simulations, probably due to limited domain size and simulation time. Most of our data are in the laminar Reynolds number regime, therefore our correlations change little when the data for the turbulent Reynolds number regime are discarded. Our lift model is questionable, for the cases where the flow is turbulent, or the flow is unstable or the particle undergoes the unsteady motion in the streamwise or lateral direction (Asmolov *et al.* 2021), since our lift force is obtained by fixing the lateral position and slip velocity, and the flow is in steady state. So far, it is conventional to directly include the lift force in the unsteady equations of particle motion. Clearly, lift models for the complex situations need further investigation.

Acknowledgements. The work was supported by the National Natural Science Foundation of China (12332015), and the Natural Science Foundation of Zhejiang Province (LZ23A020006).

Declaration of interests. The authors report no conflict of interest.

References

Adoua, R., Legendre, D. & Magnaudet, J. 2009 Reversal of the lift force on an oblate bubble in a weakly viscous linear shear flow. *J. Fluid Mech.* **628**, 23–41.

Asmolov, E.S. 1990 Dynamics of a spherical particle in a laminar boundary layer. *Fluid Dyn.* **25** (6), 886–890.

Asmolov, E.S. 1999 The inertial lift on a spherical particle in a plane Poiseuille flow at large channel Reynolds number. *J. Fluid Mech.* **381**, 63–87.

Asmolov, E.S., Dubov, A.L., Nizkaya, T.V., Harting, J. & Vinogradova, O.I. 2018 Inertial focusing of finite-size particles in microchannels. *J. Fluid Mech.* **840**, 613–630.

Asmolov, E.S., Nizkaya, T.V., Harting, J. & Vinogradova, O.I. 2021 Instability of particle inertial migration in shear flow. *Phys. Fluids* **33** (9), 092008.

Auton, T.R. 1987 The lift force on a spherical body in a rotational flow. *J. Fluid Mech.* **183**, 199–218.

Bagchi, P. & Balachandar, S. 2002 Effect of free rotation on the motion of a solid sphere in linear shear flow at moderate *Re*. *Phys. Fluids* **14** (8), 2719–2737.

Bai, B., Jin, H., Liu, P., Wang, W. & Zhang, J. 2022 Experimental study on the equilibrium position of a falling sphere in a circular tube flow. *Intl J. Multiphase Flow* **153**, 104112.

Ben Salem, M. & Oesterle, B. 1998 A shear flow around a spinning sphere: numerical study at moderate Reynolds numbers. *Intl J. Multiphase Flow* **24** (4), 563–585.

https://doi.org/10.1017/jfm.2026.11397 Published online by Cambridge University Press

CANTWELL, C.D. *et al.* 2015 Nektar++: an open-source spectral/*hp* element framework. *Comput. Phys. Commun.* **192**, 205–219.

CHERUKAT, P. & MCLAUGHLIN, J.B. 1994 The inertial lift on a rigid sphere in a linear shear flow field near a flat wall. *J. Fluid Mech.* **263**, 1–18.

CHERUKAT, P., MCLAUGHLIN, J.B. & DANDY, D.S. 1999 A computational study of the inertial lift on a sphere in a linear shear flow field. *Intl J. Multiphase Flow* **25** (1), 15–33.

EKANAYAKE, N.I.K., BERRY, J.D. & HARVIE, D.J.E. 2021 Lift and drag forces acting on a particle moving in the presence of slip and shear near a wall. *J. Fluid Mech.* **915**, A103.

EKANAYAKE, N.I.K., BERRY, J.D., STICKLAND, A.D., DUNSTAN, D.E., MUIR, I.L., DOWER, S.K. & HARVIE, D.J.E. 2020 Lift and drag forces acting on a particle moving with zero slip in a linear shear flow near a wall. *J. Fluid Mech.* **904**, A6.

GAO, W., SHI, P., PARSANI, M. & COSTA, P. 2024 On the relevance of lift force modelling in turbulent wall flows with small inertial particles. *J. Fluid Mech.* **988**, A47.

HO, B.P. & LEAL, L.G. 1974 Inertial migration of rigid spheres in two-dimensional unidirectional flows. *J. Fluid Mech.* **65** (2), 365–400.

HOMANN, H., BEC, J. & GRAUER, R. 2013 Effect of turbulent fluctuations on the drag and lift forces on a towed sphere and its boundary layer. *J. Fluid Mech.* **721**, 155–179.

HOOD, K., LEE, S. & ROPER, M. 2015 Inertial migration of a rigid sphere in three-dimensional Poiseuille flow. *J. Fluid Mech.* **765**, 452–479.

HUR, S.C., MACH, A.J. & DI CARLO, D. 2011 High-throughput size-based rare cell enrichment using microscale vortices. *Biomicrofluidics* **5**, 022206.

KIM, I. 2006 Forces on a spherical particle in shear flow at intermediate Reynolds numbers. *Intl J. Comput. Fluid Dyn.* **20** (2), 137–141.

KIM, J., CHOI, H., PARK, H. & YOO, J.Y. 2014 Inverse Magnus effect on a rotating sphere: when and why. *J. Fluid Mech.* **754**, R2.

KRAY, T., FRANKE, J. & FRANK, W. 2005 Magnus effect on a rotating sphere at high Reynolds numbers. *J. Wind Engng Ind. Aerodyn.* **110**, 1–9.

KUROSE, R. & KOMORI, S. 1999 Drag and lift forces on a rotating sphere in a linear shear flow. *J. Fluid Mech.* **384**, 183–206.

LEE, H. & BALACHANDAR, S. 2010 Drag and lift forces on a spherical particle moving on a wall in a shear flow at finite *Re*. *J. Fluid Mech.* **657**, 89–125.

LEGENDRE, D. & MAGNAUDET, J. 1997 A note on the lift force on a spherical bubble or drop in a low-Reynolds-number shear flow. *Phys. Fluids* **9** (11), 3572–3574.

LEGENDRE, D. & MAGNAUDET, J. 1998 The lift force on a spherical bubble in a viscous linear shear flow. *J. Fluid Mech.* **368**, 81–126.

LIGHTHILL, M.J. 1956 Drift. *J. Fluid Mech.* **1** (1), 31–53.

MAGNAUDET, J., RIVERO, M. & FABRE, J. 1995 Accelerated flows past a rigid sphere or a spherical bubble. Part 1. Steady straining flow. *J. Fluid Mech.* **284**, 97–135.

MAGNAUDET, J., TAKAGI, S. & LEGENDRE, D. 2003 Drag, deformation and lateral migration of a buoyant drop moving near a wall. *J. Fluid Mech.* **476**, 115–157.

MATAS, J.-P., MORRIS, J.F. & GUAZZELLI, E. 2004 Inertial migration of rigid spherical particles in Poiseuille flow. *J. Fluid Mech.* **515**, 171–195.

MATAS, J.-P., MORRIS, J.F. & GUAZZELLI, E. 2009 Lateral force on a rigid sphere in large-inertia laminar pipe flow. *J. Fluid Mech.* **621**, 59–67.

MCLAUGHLIN, J.B. 1991 Inertial migration of a small sphere in linear shear flows. *J. Fluid Mech.* **224**, 261–274.

MCLAUGHLIN, J.B. 1993 The lift on a small sphere in wall-bounded linear shear flows. *J. Fluid Mech.* **246**, 249–265.

MEI, R. 1992 An approximate expression for the shear lift force on a spherical particle at finite Reynolds number. *Intl J. Multiphase Flow* **18** (1), 145–147.

MUTO, M., TSUBOKURA, M. & OSHIMA, N. 2012 Negative Magnus lift on a rotating sphere at around the critical Reynolds number. *Phys. Fluids* **24** (1), 014102.

NAKAYAMA, S., YAMASHITA, H., YABU, T., ITANO, T. & SUGIHARA-SEKI, M. 2019 Three regimes of inertial focusing for spherical particles suspended in circular tube flows. *J. Fluid Mech.* **871**, 952–969.

SAFFMAN, P.G. 1965 The lift on a small sphere in a slow shear flow. *J. Fluid Mech.* **22** (2), 385–400.

SCHONBERG, J.A. & HINCH, E.J. 1989 Inertial migration of a sphere in Poiseuille flow. *J. Fluid Mech.* **203**, 517–524.

SEGRÉ, G. & SILBERBERG, A. 1961 Radial particle displacements in Poiseuille flow of suspensions. *Nature* **189** (4760), 209–210.

https://doi.org/10.1017/jfm.2026.11397 Published online by Cambridge University Press

SHAO, X., YU, Z. & SUN, B. 2008 Inertial migration of spherical particles in circular Poiseuille flow at moderately high Reynolds numbers. *Phys. Fluids* **20** (10), 103307.
SHI, P., CLIMENT, É. & LEGENDRE, D. 2024 Lift force on a spherical droplet in a viscous linear shear flow. *J. Fluid Mech.* **1000**, A88.
SHI, P. & RZEHAK, R. 2019 Lift forces on solid spherical particles in unbounded flows. *Chem. Engng Sci.* **208**, 115145.
SHI, P., RZEHAK, R., LUCAS, D. & MAGNAUDET, J. 2021 Drag and lift forces on a rigid sphere immersed in a wall-bounded linear shear flow. *Phys. Rev. Fluids* **6** (10), 104309.
TAKEMURA, F. & MAGNAUDET, J. 2003 The transverse force on clean and contaminated bubbles rising near a vertical wall at moderate Reynolds number. *J. Fluid Mech.* **495**, 235–253.
TAKEMURA, F., MAGNAUDET, J. & DIMITRAKOPOULOS, P. 2009 Migration and deformation of bubbles rising in a wall-bounded shear flow at finite Reynolds number. *J. Fluid Mech.* **634**, 463.
TAKEMURA, F., TAKAGI, S., MAGNAUDET, J. & MATSUMOTO, Y. 2002 Drag and lift forces on a bubble rising near a vertical wall in a viscous liquid. *J. Fluid Mech.* **461**, 277–300.
VASSEUR, P. & COX, R.G. 1976 The lateral migration of a spherical particle in two-dimensional shear flows. *J. Fluid Mech.* **78** (2), 385–413.
VASSEUR, P. & COX, R.G. 1977 The lateral migration of spherical particles sedimenting in a stagnant bounded fluid. *J. Fluid Mech.* **80** (3), 561.
WANG, T., LIN, Z., GUO, Y. & YU, Z. 2025 Hydrodynamic forces on a spherical particle in a plane Couette flow. *Intl J. Multiphase Flow* **192**, 105341.
WEI, M., DUAN, J., WANG, X. & ZHOU, J. 2023 Motion of a solid particle in an ore-lifting riser with transverse vibrations. *Phys. Fluids* **35** (11), 113311.
YAHIAOUI, S. & FEUILLEBOIS, F. 2010 Lift on a sphere moving near a wall in a parabolic flow. *J. Fluid Mech.* **662**, 447–474.
YANG, B.H., WANG, J., JOSEPH, D.D., HU, H.H., PAN, T.-W. & GLOWINSKI, R. 2005 Migration of a sphere in tube flow. *J. Fluid Mech.* **540**, 109–131.
YU, Z., PHAN-THIEN, N. & TANNER, R.I. 2004 Dynamic simulation of sphere motion in a vertical tube. *J. Fluid Mech.* **518**, 61–93.
ZENG, L., NAJJAR, F., BALACHANDAR, S. & FISCHER, P. 2009 Forces on a finite-sized particle located close to a wall in a linear shear flow. *Phys. Fluids* **21** (3), 033302.

https://doi.org/10.1017/jfm.2026.11397 Published online by Cambridge University Press